

Influence of Specific Energy Inhomogeneity on the CO₂ Splitting Performance in a High-Power Plasma Jet

Hendrik Burghaus, Clemens F. Kaiser, Stefan Fasoulas, Georg Herdrich

^aInstitute of Space Systems (IRS), University of Stuttgart, Pfaffenwaldring 29, Stuttgart, 70569, Baden-Württemberg, Germany

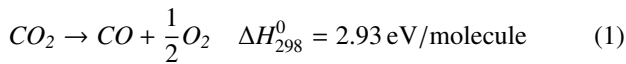
Abstract

Plasma-based CO₂ conversion is a promising pathway towards greenhouse gas recycling. In the corresponding research field, various types of plasma reactors are applied for carbon dioxide dissociation. So far, spatial inhomogeneities of the specific energy (SEI) distribution in plasma generators, e.g., induced by non-uniform heating or an inhomogeneous mass distribution, are not the focus of the investigations. In this work, the spatial inhomogeneity of mass-specific enthalpy in the plasma jet of the inductive plasma generator IPG4 at the Institute of Space Systems (IRS) is examined. For this purpose, the mean mass-specific enthalpy as well as the radial distribution of the local enthalpy are measured using plasma probes. Moreover, the influence of the determined specific enthalpy inhomogeneity on the CO₂ splitting performance is quantified. It is shown that an inhomogeneous radial distribution of the specific energy can significantly lower the carbon dioxide conversion, compared to a homogeneous case. With regards to IPG4, the performance reduction is 16 %.

Keywords: inductively coupled plasma, plasma diagnostics, CO₂ splitting, plasma technology, plasma wind tunnel

1. Introduction

The fundamental role of anthropogenic greenhouse gas (GHG) emissions in the relentlessly progressing climate change on Earth is undeniable. Therefore, the Intergovernmental Panel on Climate Change (IPCC) sees a massive reduction in GHG emissions as the only way to limit global warming to 1.5 °C or even 2.0 °C. In the IPCC's sixth assessment report, Carbon Capture and Utilization (CCU) and Carbon Capture and Storage (CCS) are defined as necessary tools for the mitigation of carbon dioxide emissions [1]. To this end, plasma technology might be a promising way of converting CO₂ into value-added compounds [2]. One fundamental process under investigation is the plasma-based conversion of pure carbon dioxide into the syngas carbon monoxide and oxygen, called CO₂ splitting [3]:



Major advancements have been made in the application of non-thermal plasmas (NTP) for CO₂ splitting, with and without catalyst [4]. Besides NTP, also the dissociation of CO₂ in thermodynamic equilibrium is increasingly subject of research, as it could be demonstrated that thermal reactions dominate the CO₂ conversion in microwave (MW) and gliding arc (GA) plasmas [2]. Here, several ways to overcome the energy efficiency limit of around 50 % [3] have been identified, such as superideal chemical quenching by O-CO₂ association [5] or thermal quenching by fast expansion through a de Laval nozzle [6, 7].

A great part of the research is focused on the reaction kinetics, especially the excitation of vibrational modes of carbon dioxide. In this context of plasma-based CO₂ splitting, the spe-

cific energy input (SEI) has been identified as a key parameter, which is commonly expressed in units of eV/molecule [3]:

$$\text{SEI}[\text{eV/molecule}] = \frac{P_{\text{cal}}}{\dot{m}_{\text{CO}_2}} \cdot \frac{M_{\text{CO}_2}}{e \cdot N_A} \quad (2)$$

Here, P_{cal} is the plasma power, \dot{m}_{CO_2} the mass flow rate of carbon dioxide, M_{CO_2} is the molar mass of CO₂, e is the elementary charge and N_A is the Avogadro's constant. In the shown formulation, Eq. 2 is applicable for a pure carbon dioxide gas. While current research concentrates on the optimization of the specific energy input, not much can be found on spatial inhomogeneities of the SEI in a plasma jet in literature. Wolf et al. numerically simulate non-uniform heating in a MW plasma generator and stress the importance of local SEI measurements in contrast to the commonly used global values [8]. To date, local effects are barely understood, especially from the experimental side. Nevertheless, the occurrences of SEI inhomogeneities are described in a variety of studies. Possible origins of the inhomogeneities are a spatially non-uniform power distribution in the discharge region, heterogeneous distribution of the mass flux, expansion of the plume, wall cooling effects, magnetohydrodynamic (MHD) effects, or, as is usually the case, the combination of several of these. In general, most types of plasma generators are expected to show spatial SEI inhomogeneities due to a complex superposition of mass flux and power distribution. In this regard, Bogaerts and Centi state that in GA plasmas only a fraction of the gas passes the discharge, which limits the conversion [2]. Moreover, contraction phenomena are known to be a limiting factor in MW plasmas [2, 9] with respect to carbon dioxide conversion.

At the Institute of Space Systems (IRS), the plasma wind tunnel PWK3, powered by the inductive plasma generator IPG4, is

used for experimental investigations on thermal CO₂ splitting at high powers. Specific energy inhomogeneities in the plasma jet of PWK3 are known and measured for two decades already (e.g., [10, 11, 12, 13, 14]). Moreover, mean specific enthalpies are reported for pure oxygen flows in PWK3 by Herdrich [15]. Only recently with the investigations on CO₂ splitting at IRS ([16, 14]), the correlation between radially distributed local specific energy and integral values in PWK3 moved into focus.

It has to be noted that in the field of plasma wind tunnels, the energy per particle in the plasma is labeled as total mass-specific enthalpy h_{tot} . This measure is the same as the specific energy input, but usually specified in different units:

$$h_{\text{tot}}[\text{J/kg}] = SEI[\text{eV/molecule}] \frac{e \cdot N_A}{M_{\text{CO}_2}} = \frac{P_{\text{cal}}}{\dot{m}_{\text{CO}_2}} \quad (3)$$

In accordance with Eq. 2), P_{cal} is the plasma power and \dot{m}_{CO_2} the mass flow rate of carbon dioxide. In the course of this work, the terms specific energy input, specific energy, mass-specific enthalpy and specific enthalpy are used interchangeably. The parameters SEI and h_{tot} are applied for the expression of the same quantity in units of [eV/molecule] and [J/kg], respectively.

In this paper, the influence of spatial (radial) specific energy inhomogeneities in the plasma jet of the inductive plasma generator IPG4 on the carbon dioxide splitting performance is examined by comparing integral measurements of the mean (bulk) enthalpy and locally measured mass-specific enthalpy values.

In Section 2, the experimental facility as well as the plasma probes used in the course of this work are introduced. Furthermore, a software tool for thermal carbon dioxide splitting is described. Section 3 contains the measurement results of mean and local enthalpies. Moreover, the influence of specific energy inhomogeneities on the CO₂ splitting performance is investigated by a parameter study.

2. Experimental setup and tools

At the Institute of Space Systems (IRS) three plasma wind tunnels are operated to experimentally simulate the entry of objects into planetary atmospheres [17]. All experiments in the course of this work are conducted in the plasma wind tunnel PWK3, powered by the inductively coupled plasma generator IPG4. In the following, the experimental setup of PWK3 and the applied intrusive plasma diagnostics are described. Moreover, the concept of carbon dioxide splitting in thermodynamic equilibrium is introduced.

2.1. Experimental facility

The plasma wind tunnel PWK3 consists of a stainless-steel vacuum chamber with a diameter of 1.6 m and a length of 2 m, as well as an inductive plasma generator (IPG3). In the case of CO₂ operation a convergent nozzle is attached to the plasma source, then called IPG4. A schematic of the facility is shown in Fig. 1.

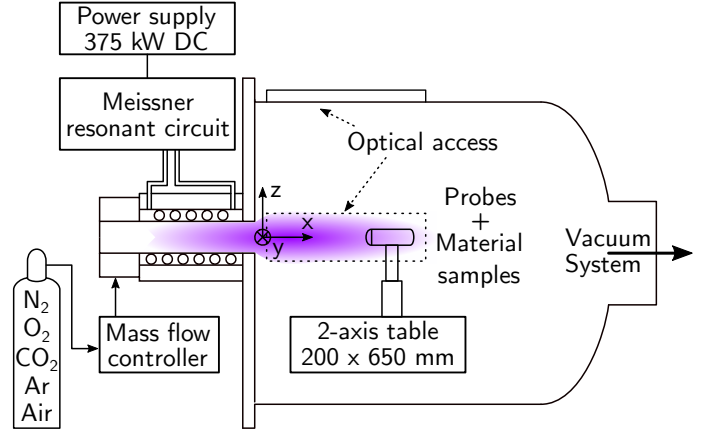


Figure 1: Schematic of plasma wind tunnel PWK3 with probe installed.

The vacuum chamber is connected to a centralized vacuum system [17]. Several optical access points allow for non-intrusive diagnostics and visual monitoring. Moreover, a water-cooled probe and material sample-holder can be mounted on a numerically controlled two-axis table in the tank center, e.g., for intrusive measurements and material testing. The reference coordinate system of PWK3 is marked in Fig. 1. Its origin ($x = 0$ mm) lies in the generator exit plane, but for reasons of readability it is shifted to the right in the figure.

The plasma generator IPG4, connected to the tank lid, is powered by an external power supply. Together with a resonant circuit consisting of up to seven 6 nF capacitors and the IPG inductance coil the power supply delivers an anode power of 180 kW maximum. A 2.0 mm thick quartz tube, surrounded by a copper coil of 5.5 turns, forms the discharge channel of IPG4. The convergent nozzle attached to IPG4 has a length of 35 mm and a throat diameter of 50 mm. Thus, the nozzle exit plane lies at $x = 35$ mm. The coil, quartz tube and nozzle are cooled by high-pressure water.

Figure 2 shows a schematic of the inductive plasma generator, as well as a photograph (Sony A6400) of a heat flux measurement in a pure CO₂ jet in PWK3.

The electrodeless plasma generation in IPG4 allows for the operation of PWK3 with a large variety of gases, including pure oxygen and carbon dioxide. The high plasma purity enables investigations on gas-surface interactions, e.g., for thermal protection system (TPS) materials ([18, 13, 19]). In this work, a range of operating conditions of PWK3 with carbon dioxide is studied. A summary can be found in Tab. 1.

In the context of this paper, the maximum operational range of IPG4 with regards to the mean mass-specific enthalpy is characterized. This is achieved by variation of the anode power between 135 kW and 160 kW, and variation of the mass flow rate between 2.2 g/s and 4.0 g/s. The limitations on that range stem from laboratory safety regulations, as well as the generator discharge stability. Except for the mass flow rate and anode power, the facility parameters are kept constant. The changes in anode voltage and injector pressures are directly connected to the change in specific energy. The tank pressure is adjusted actively by the injection of molecular nitrogen at the back of the

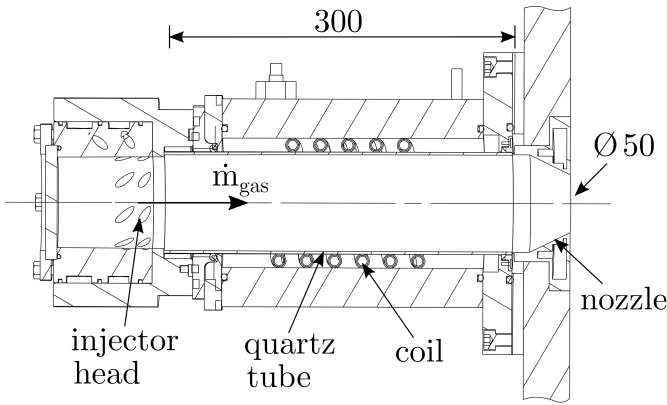


Figure 2: Schematic of the inductive plasma generator IPG4 (left) and photograph of its CO₂ plasma plume during heat flux measurements at $\dot{m}_{\text{CO}_2} = 2.2 \text{ g/s}$, $P_A = 160 \text{ kW}$ and $p_{\text{amb}} = 100 \text{ Pa}$ in PWK3 (right).

Table 1: Range of operating conditions of PWK3/IPG4 used in this work

Parameter	Symbol	Value
Anode power	P_A	135 – 160 kW
Anode voltage	U_A	6600 – 6950 V
Number of capacitors	n_k	6
Coil turns	n_{coil}	5.5
Operational frequency	f	520 kHz
Quartz tube thickness	th_{tube}	2.0 mm
Attached nozzle	-	convergent
Ambient pressure	p_{amb}	30 – 100 Pa
Injector pressure	p_{inj}	2855 – 3720 Pa
Mass flow rate [CO ₂]	\dot{m}_{CO_2}	2.2 – 4.0 g/s

vacuum tank. Detailed information on the investigated combinations of mass flow rate and anode power will be given in Tab. 2 in Section 3.1.

2.2. Plasma diagnostics

As mentioned in Section 1, this paper deals with spatial inhomogeneities in the mass-specific enthalpy of a carbon dioxide plasma jet, meaning the distribution of energy per particle over the radius. Consequently, the analysis is based on the comparison of the mean (bulk) enthalpy of the whole plume and locally measured values. For this purpose, two types of intrusive plasma probes, the cavity calorimeter for integral measurements and the heat flux-Pitot double probe for radially resolved measurements, are applied. Both setups and the underlying working principles of the probes are explained in the following.

2.2.1. Heat flux-Pitot double probe

To determine a radial profile of local mass-specific enthalpies in the CO₂ plasma jet of IPG4 the so-called heat flux-Pitot double probe is used. The measurements are performed at an axial distance of $x = 156 \text{ mm}$ from the generator exit, which equals a distance of 121 mm to the nozzle exit. This test position is chosen for reasons of comparison to measurements performed

in the past [14]. A schematic of the double probe is shown in Fig. 3.

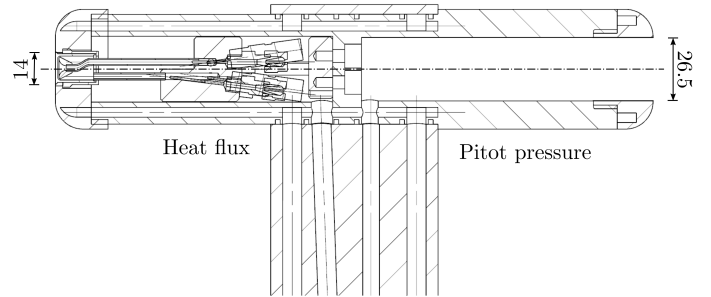


Figure 3: Sectional view of the heat flux-Pitot double probe with the 14 mm copper calorimeter insert on the left and the 26.5 mm Pitot tube on the right.

The two-sided probe is capable of measuring the heat flux and the Pitot pressure at the test position, depending on which side of the probe is facing the plasma. Both probe heads have an outer diameter of 50 mm. On the left side (Fig. 3) the heat flux on a thermally insulated copper oxide surface with a diameter of 14 mm is measured calorimetrically. The heat flux insert is water-cooled and the water volume flow is monitored by a Siemens Sitrans FM MAG 1100/5000 sensor system. Moreover, the temperature difference of the in- and out-flowing water ΔT_w is measured by two Pt100 sensors inside the probe. Together with the known heat capacity $c_{p,w}$, the water mass density ρ_w and the calorimeter surface area A_{cal} , the calorimetric heat flux on the copper surface \dot{q}_{cal} can be determined as:

$$\dot{q}_{\text{cal}} = \frac{\rho_w \dot{V}_w}{A_{\text{cal}}} c_{p,w} \Delta T_w \quad (4)$$

Opposite of the calorimeter probe head is a Pitot tube with a diameter of 26.5 mm. The Pitot pressure is measured with a pressure gauge (MKS 122AAX-00100DBS) connected to the Pitot side of the double probe. The same gauge is used for the determination of the tank pressure at all test conditions in this work. Together, the local stagnation pressure and the calorimetrically determined heat flux allow for an approximation of the

local mass-specific enthalpy h_{tot} , as formulated by Marvin and Pope [20]:

$$h_{\text{tot}} - h_w = \frac{1}{K_i} \frac{\dot{q}_{\text{fc}}}{\sqrt{\left(\frac{p_{\text{pitot}}}{R_{\text{eff}}}\right)}} \quad (5)$$

Here, K_i denotes a gas specific constant, which is adopted from Zoby as $0.4337 \text{ kWkg}/(\text{m}^{3/2} \text{ Pa}^{1/2} \text{ MJ})$ for CO_2 [21, 22]. The parameter \dot{q}_{fc} represents the fully catalytic heat flux and R_{eff} the effective nose radius, which is 2.3 times the body radius $R_b = 25 \text{ mm}$ for the double probe used in the course of this work [20]. In this analysis, the wall enthalpy h_w is neglected and the measured heat flux is assumed to be fully catalytic, based on past investigations at IRS by Marynowski et al. [12].

2.2.2. Cavity calorimeter

In order to measure the bulk enthalpy of the plasma jet in PWK3, a so-called cavity calorimeter was developed at the Institute of Space Systems [15]. The basic idea behind this probe is to trap the whole plasma jet inside the calorimeter. Constant water cooling of the probe induces full relaxation of the gas temperature, chemical potential and flow velocity, allowing for the calorimetric determination of the plasma power. The cavity calorimeter is mounted to the probe holder in PWK3 and placed at a distance of $x = 100 \text{ mm}$ to the generator exit. This value was determined to be optimal for capturing the entire plasma jet, with no significant residual plasma flow around the probe, which would falsify the measurements, and without disturbing the discharge in the generator [15]. Once positioned in front of the generator exit, the calorimeter was not moved anymore and the ignition was done with the probe in place already. In Fig. 4 a schematic of the cavity calorimeter is shown.

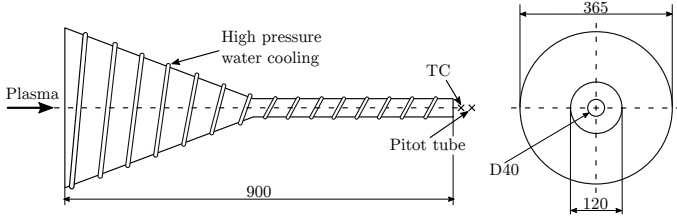


Figure 4: Schematic of the cavity calorimeter, including the placement of the thermocouple (TC) and the Pitot tube at the exit.

The cone-shaped calorimeter with a length of 900 mm is made out of copper. Its inlet, a circular orifice, has a diameter of 120 mm, which is more than double the size of the IPG4 nozzle exit. The calorimeter cone is followed by a cylindrical tube of 40 mm diameter at the end of which the cooled gas exits the probe. All calorimeter surfaces are cooled by water in spiral copper tubes on the inside and outside. The water flow rate is monitored by a Siemens Sitrans FM MAG 1100/5000 sensor system. Moreover, the inflow and outflow temperatures of the cooling water are measured with two Pt100 sensors (not shown in Figure 4). In addition to the original test setup (see [15]) the cavity calorimeter is complemented by a Type K thermocouple (TC) and a Pitot tube, which are placed at the calorimeter end,

inside the exiting gas stream. Later it will be shown that these additional diagnostics allow for the determination of the residual enthalpy content of the exiting gas and, thus, for a more accurate determination of the plasma jet power.

The methodology behind the data analysis is based on Herdrich [23, 15] and has been advanced in the course of this work. Generally, the cavity calorimeter is able to measure the total mean enthalpy of the plasma, introduced by the generator:

$$\bar{h}_{\text{tot}} = \int_{300 \text{ K}}^T c_p dT + (h_{\text{chem}} - \Delta H_f^0) + \frac{1}{2} u_{\infty}^2 \quad (6)$$

Here, c_p and T are the specific heat capacity and the gas temperature of the plasma, respectively. The chemical potential is denoted by h_{chem} . This is corrected by the standard enthalpy of formation of the gas ΔH_f^0 in order to get the enthalpy that is coupled by the plasma generator, without considering the production of CO_2 itself. This way, the mass-specific enthalpy is zero for a carbon dioxide gas at 300 K, i.e., the feed gas of the generator. As the last contribution to the total enthalpy, the mass-specific kinetic energy is represented by the flow velocity u_{∞} .

From the principle of operation, the cavity calorimeter measures power, not enthalpy. In this work, the total calorimetric plasma power P_{cal} is determined by combining the calorimeter, TC and Pitot tube measurements. Radiation losses of the calorimeter are assumed to be one percent, in accordance with [15], to stay consistent with research conducted in the past.

$$P_{\text{cal}} = 1.01 \cdot P_{\text{cavity}} + P_{\text{heat,exit}} + P_{\text{kin,exit}} \quad (7)$$

In addition to the plasma power measured by the cavity calorimeter P_{cavity} , the thermal power $P_{\text{heat,exit}}$ and the kinetic power $P_{\text{kin,exit}}$ left in the gas at the calorimeter exit are considered. The calorimeter power is calculated similarly to the heat flux of the double probe (Eq. 4), but for the entire plasma jet at once rather than locally:

$$P_{\text{cavity}} = \rho_w c_{p,w} \dot{V}_w (T_{\text{out}} - T_{\text{in}}) \quad (8)$$

To estimate the thermal power at the exit, the mass flow rate \dot{m}_{exit} and the mass-specific enthalpy of the cooled gas h_{exit} must be known:

$$P_{\text{heat,exit}} = \dot{m}_{\text{exit}} h_{\text{exit}}(p_{\text{amb}}, T_{\text{exit}}) \quad (9)$$

For this, thermodynamic equilibrium is assumed at the calorimeter exit. The software toolkit Cantera [24] is used to calculate the specific enthalpy based on the measured gas temperature at the exit. More information on these type of simulations will be given in Section 2.3. Furthermore, the static pressure at the exit is set equal to the ambient pressure in the tank. Since the exit mass flow rate is not measured, it is assumed to be equal to the initial mass flow rate in IPG4. The underlying assumption here is that the plasma jet is captured completely inside the calorimeter.

The kinetic power of the exiting gas completes the analysis and is determined as follows:

$$P_{\text{kin,exit}} = \frac{1}{2} \dot{m}_{\text{exit}} u_{\text{exit}}^2 \quad (10)$$

Here, the flow velocity of the exiting gas u_{exit} is calculated combining the measured gas temperature and the Mach number at the exit. The Mach number itself is calculated via the Rayleigh Pitot formula [25], using the stagnation pressure measured with the Pitot tube. For subsonic conditions the simpler isentropic flow equation must be applied.

During the operation of plasma wind tunnel PWK3 significant power losses occur due to cooling of the quartz tube of the generator and the convergent nozzle attached to it. The IPG4 quartz tube cooling power Q_{tube} is monitored constantly for each test performed. Moreover, measurements of the nozzle cooling power Q_{nozzle} for all conditions investigated in the course of this work were performed. Both cooling losses are measured calorimetrically. Together with the measured calorimetric plasma power, important generator/facility efficiencies can be derived. The definitions of the efficiencies are based on Dropmann and Herdrich [26, 23] and summarized in the following.

The coupling efficiency describes how much power is coupled into the working gas, compared to the power applied to the anode. This includes the calorimetric plasma power, the tube cooling and the nozzle cooling:

$$\eta_{\text{couple}} = \frac{P_{\text{cal}} + Q_{\text{tube}} + Q_{\text{nozzle}}}{P_A} \quad (11)$$

The tube cooling contains a small amount of heat generated in the IPG4 copper coil that is not coupled to the plasma and should be excluded in Eq. 11. However, due to the negligible size of that coil heating (order of Watts), no correction is applied. The thermal efficiency states how much of the coupled power is lost due to cooling of the generator discharge channel and the convergent nozzle:

$$\eta_{\text{th}} = \frac{P_{\text{cal}}}{P_{\text{cal}} + Q_{\text{tube}} + Q_{\text{nozzle}}} \quad (12)$$

Most importantly, the total efficiency is the ratio of the calorimetric plasma power, i.e., the power actually present in the gas in the vacuum chamber, to the anode power:

$$\eta_{\text{tot}} = \eta_{\text{couple}} \cdot \eta_{\text{th}} = \frac{P_{\text{cal}}}{P_A} \quad (13)$$

Extensive studies on the PWK3 efficiencies for pure oxygen plasmas by Herdrich can be found in [10]. The current paper represents the first measurement of the plasma power and the facility efficiencies for a carbon dioxide plasma in PWK3 (see Section 3.1).

2.3. CO_2 splitting in thermodynamic equilibrium

Heating carbon dioxide up to temperatures of several thousand degrees leads to decomposition of the otherwise stable molecule. This splitting process in thermochemical equilibrium is the simplest route of CO_2 dissociation, but is generally limited with regards to energy efficiency as mentioned in Section 1. In this work, a code has been developed, based on the software toolkit Cantera [24], to simulate the process of thermal carbon dioxide splitting at a given pressure. This includes the splitting performance parameters, like specific energy input (SEI), the

CO_2 conversion χ and the energy efficiency η . The definitions of the CO_2 splitting performance parameters follow Snoeckx et al. [3], but with adaptation to the applications in this paper. In the context of this work, ideal quenching without heat recovery is assumed. The conversion of carbon dioxide is defined as the ratio of converted to the initial CO_2 mass:

$$\chi = \frac{m_{\text{CO}_2,0} - m_{\text{CO}_2}}{m_{\text{CO}_2,0}} = \frac{m_{\text{CO}_2,\text{converted}}}{m_{\text{CO}_2,0}} \quad (14)$$

with the initial and current carbon dioxide masses being $m_{\text{CO}_2,0}$ and m_{CO_2} , respectively. In the case of thermodynamic equilibrium CO_2 splitting, "current" refers to the state after heating. Consequently, the energy efficiency is defined as:

$$\eta = \chi \cdot \frac{\Delta H_{298}^0}{SEI} = \chi \cdot \frac{\Delta H_{298}^0}{h_{\text{tot}}} \frac{e \cdot N_A}{M_{\text{CO}_2}} \quad (15)$$

with the CO_2 conversion χ and the standard reaction enthalpy for carbon dioxide splitting $\Delta H_{298}^0 = 2.93 \text{ eV/molecule}$ [3]. In Fig. 5 the composition and splitting performance of a CO_2 gas in thermodynamic equilibrium are plotted. The pressure in the simulation is 2900 Pa, representative for the injector pressure of IPG4 at the lowest mass flow rate of 2.2 g/s and an anode power of 160 kW.

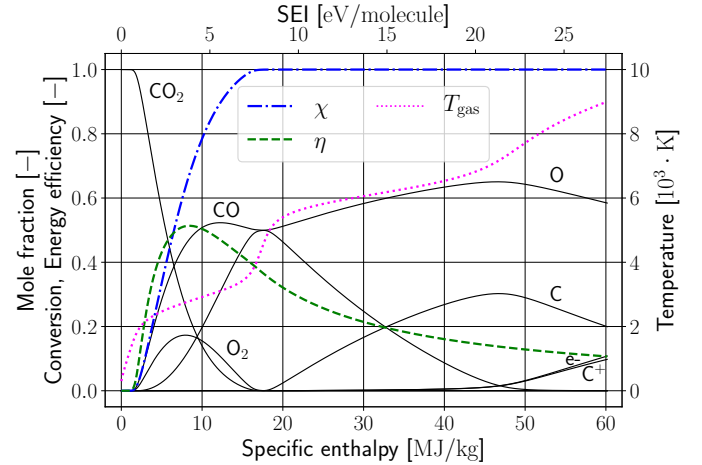


Figure 5: Composition and splitting performance of a CO_2 gas in thermodynamic equilibrium as a function of specific enthalpy at 2900 Pa. The gas temperature is shown in magenta, the conversion in blue and the energy efficiency in green.

In the figure, the specific energy input in eV/molecule is plotted as a secondary x-axis for reasons of convenience. The gas composition is depicted as black lines. At approx. 16 MJ/kg the dissociation of carbon dioxide is completed, which is reflected in the conversion (blue) approaching 100%. Consequently, at higher enthalpies carbon monoxide decomposition and ionization, mostly of atomic carbon, takes place. The gas temperature, which is very sensitive to the static pressure, reaches approx. 3500 K at full CO_2 dissociation and rises to 9000 K at an enthalpy of 60 MJ/kg. The energy efficiency reaches its maximum of approx. 51% at an enthalpy of 8.4 MJ/kg. Again, it has to be emphasized that the CO_2 splitting performance is calculated under the assumption of ideal quenching without heat recovery.

3. Results and discussion

As this paper strives to investigate the influence of a spatially inhomogeneous distribution of the specific energy (mass-specific enthalpy) on the CO₂ splitting performance, the mandatory first step is to show and quantify the spatial inhomogeneity in PWK3. In the following, this is done by using the plasma diagnostic probes introduced in Section 2. Subsequently, the influence of the measured inhomogeneity on the carbon dioxide splitting performance in IPG4 is analyzed in Section 3.2. The majority of the data analysis is performed in Python using the NumPy [27], Matplotlib [28], SciPy [29] and Pandas [30] packages.

3.1. Plasma jet characterization

The characterization of the IPG4 plasma jet is split into two parts. First, the mean enthalpy of the entire jet, as well as the generator efficiencies, are determined with the cavity calorimeter. Five different test conditions in a wide operational range of IPG4 are analyzed. Second, for one of these conditions (CO2#01b) the radial distribution of local mass-specific enthalpy values is measured with the heat flux-Pitot double probe.

3.1.1. Bulk enthalpy & generator efficiencies

In the past, extensive studies on the bulk enthalpy of oxygen plasmas in PWK3 were performed by Herdrich using the cavity calorimeter [15, 10]. The experiments conducted in the frame of this paper represent the first attempt at measuring the mean enthalpy for carbon dioxide. Moreover, the determination of the nozzle cooling power for IPG4 is a novelty. The operating parameters of the corresponding test conditions are summarized in Tab. 2. Parameters that are not part of the table are the same as in Tab. 1 for all experiments. As stated before, the anode voltage and the injector pressure are not target parameters, but their changes are the result of altering the mass flow rate and the anode power.

Table 2: Summary of test conditions for the CO₂ cavity calorimeter experiments in PWK3 at varying specific anode powers \bar{h}_A .

Condition	P_A [kW]	\dot{m}_{CO_2} [g/s]	\bar{h}_A [MJ/kg]	p_{amb} [Pa] ^a
CO2#01a	160	2.2	72.73	27
CO2#01b	160	2.2	72.73	83
CO2#02	160	3.0	53.33	92
CO2#03	150	3.5	42.86	97
CO2#04	135	4.0	33.75	102

^a Due to placement of the cavity calorimeter in front of the generator exit, the ambient pressure is not representative of the free-stream conditions.

The five test conditions are labeled as CO2#01a/b-CO2#04, differing in anode power, mass flow rate and/or tank pressure. The higher the number, the lower the ratio of applied anode power P_A and mass flow rate \dot{m}_{CO_2} , defined as \bar{h}_A :

$$\bar{h}_A = \frac{P_A}{\dot{m}_{\text{CO}_2}} \quad (16)$$

The specific anode power \bar{h}_A is by definition a representation of the facility operating conditions. Consequently, it does not account for losses and is to be distinguished from the mean specific energy coupled into the plasma:

$$\bar{h}_{\text{tot}} = \eta_{\text{tot}} \cdot \bar{h}_A \quad (17)$$

The first two conditions are the same with regards to the generator operating parameters, but differ in the tank pressure, and are distinguished by an additional lowercase letter. The tank pressure at CO2#01a is at minimum (30 Pa), while for the other conditions molecular nitrogen is injected at the back of the vacuum tank (cp. Section 2.1). The target pressure for CO2#01b - CO2#04 was 100Pa, but due to a limited test time an adjustment of the nitrogen mass flow for each condition was not possible. Moreover, capturing the plasma jet inside the cavity calorimeter influences the ambient pressure measured at the tank wall and it is not fully representative of the free-stream conditions. Nevertheless, since the ambient pressures were high enough to constrict the plasma jet to diameters smaller than the calorimeter opening, the slightly lower tank pressure is not believed to have significant influence on the cavity calorimeter measurements. In Fig. 6, the measured calorimetric plasma powers as well as the tube and nozzle cooling losses for all five conditions are illustrated.

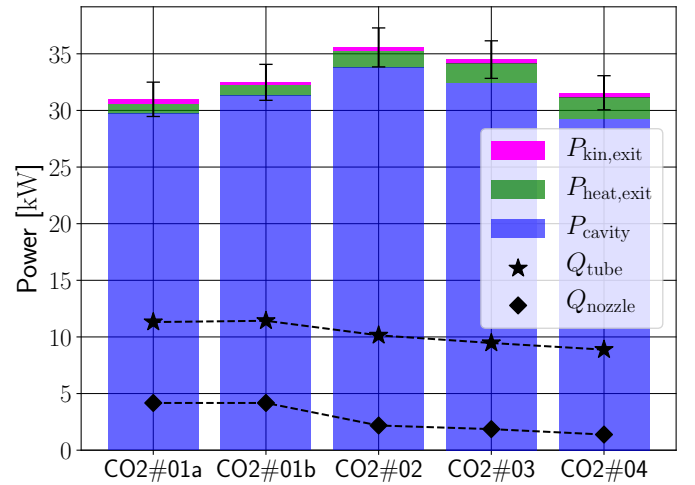


Figure 6: Measured calorimetric plasma powers for the investigated conditions. Partitions of the thermal and kinetic exit powers are shown in green and magenta, respectively. The corresponding tube and nozzle cooling powers are indicated with black stars and diamonds, respectively.

The power directly measured with the cavity calorimeter (Eq. 8]) is shown in blue, while the thermal (Eq. 9) and the kinetic (Eq. 10) powers of the gas exiting the probe are shown in green and magenta, respectively. The tube and nozzle cooling powers are plotted in black. With regards to the nozzle cooling, the first two test conditions are treated as one, since no difference could be observed. The measured calorimetric plasma powers are in the range of approx. 30 – 35 kW for all conditions. It is evident that the cavity calorimeter is able to capture most of the inherent plasma power, and only little power is left in the gas exiting the device. Nevertheless, neglecting the remaining enthalpy in the

outflowing gas causes an error of up to 7 % in the case of high mass flow rates, which justifies the improvements made to the test setup. Comparing CO2#01a and CO2#01b shows the influence of raising the ambient pressure. Not only is the measured power higher at elevated pressure, proving that capturing the whole plasma jet is not possible at minimum pressure, but also the partitions change. While the kinetic exit power decreases with increasing ambient pressure, the temperature at the exit increases. This is most likely due to the lower expansion at elevated pressure and, thus, less conversion of heat into kinetic energy. The condition CO2#02 shows the highest calorimetric plasma power. With further decreasing anode power, the calorimetric plasma power decreases, as expected. The cooling losses are significantly lower for higher mass flow rates. Reason for this is the lower energy per particle, leading to lower temperatures in the discharge. Moreover, during the experiments it could be observed that the plasma jet decouples from the nozzle with higher mass flow rates. The exact correlation between injector pressure and jet expansion is not investigated in this paper, but can be seen as a factor for the nozzle cooling reduction.

Following the methodology in Section 2.2.2, Eqs. 11-13 are applied to determine relevant efficiencies of the plasma generator IPG4 and the PWK3 facility as a whole. The coupling, thermal and total efficiencies of all five test conditions are plotted over the specific anode power in Fig. 7.

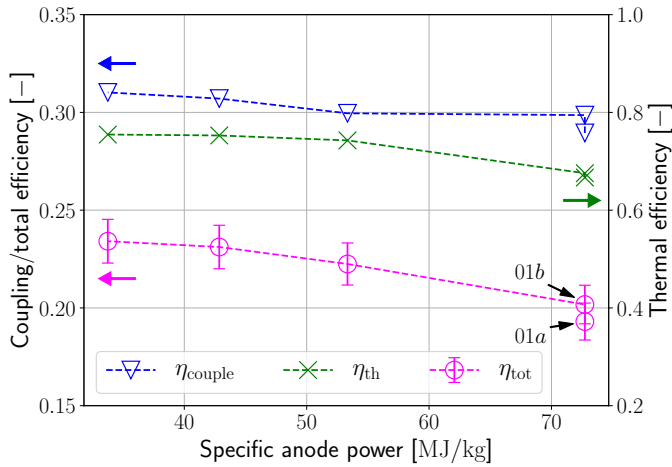


Figure 7: Measured coupling, thermal and total efficiencies plotted over the specific anode power \bar{h}_A , i.e., the ratio of anode power and mass flow rate, for test conditions CO2#01 (right) to CO#04 (left).

The thermal efficiency lies between 60 and 80 percent for all conditions. The coupling efficiency is rather low ($< 32\%$) and decreases with higher specific energies. Consequently, the total efficiency of IPG4 for pure CO₂ plasma flows ranges from approx. 20 to 25 percent, also decreasing with specific energy. The two adjacent points at the highest \bar{h}_A , i.e., CO2#01a and CO2#01b, show a jump in efficiency when increasing the ambient pressure from 30 Pa to 83 Pa. This justifies the use of elevated pressure in all experiments in order to capture the whole plasma jet inside the cavity calorimeter and avoid residual flow around the device. In contrast, the thermal efficiency is not affected by the tank pressure, indicating that the discharge in

the generator itself is unaltered. The measurement results of the cavity calorimeter experiments are summarized in Tab. 3. Here, the bulk enthalpy \bar{h}_{tot} is introduced as the ratio of calorimetrically measured plasma power and the total mass flow rate, assuming that the entire mass flux passes through the cavity calorimeter.

The measured bulk enthalpies cover an interesting range regarding thermal CO₂ splitting (Fig. 5). While the high power condition CO2#01b is expected to just about reach full conversion (97 %) at a medium high energy efficiency of 42 %, condition CO2#04 with a bulk enthalpy of 7.89 MJ/kg is near the optimum efficiency of 51 % at lower conversion of 63 %.

For oxygen plasma in PWK3, Herdrich determined a total efficiency of 22 % at $\bar{h}_A = 47.7$ MJ/kg using a 5.5 turn IPG coil and four capacitors in the resonant circuit. [15]. This corresponds well to the measured efficiencies for carbon dioxide in the course of this work. Moreover, Herdrich observed the same trend of higher total efficiencies with lower specific anode powers, reaching up to 35 % at $\bar{h}_A = 19.3$ MJ/kg [15].

3.1.2. Radial specific enthalpy distribution

In order to quantify the spatial specific energy inhomogeneity in the IPG4 CO₂ plasma jet, local measurements of the mass-specific enthalpy were conducted at an axial position of $x = 156$ mm for one condition, i.e., CO2#01b, with the heat flux-Pitot double probe. The tank pressure was set to 100 Pa for all tests. In Fig. 8 the measured heat flux, referred to the 50 mm probe geometry, as well as the Pitot pressure over the radius are shown. Due to their small size, the error bars are not drawn for reasons of readability. On the centerline, the relative errors are 4 % for the heat flux and 2 % for the Pitot pressure.

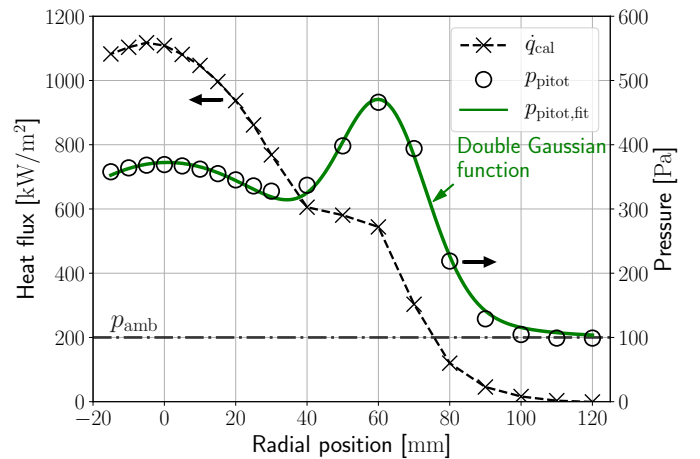


Figure 8: Radial profiles of local heat flux and Pitot pressure for the condition CO2#01b at $x = 156$ mm. A double Gaussian distribution (green line) is fitted to the Pitot values. The tank pressure of 100 Pa is indicated by a horizontal line.

Slightly left of the plasma jet centerline, a maximum heat flux of 1117 kW/m² is measured by the calorimetric insert. The small offset of the peak position to $r = 0$ mm is due to unavoidable inaccuracies in manual probe placement. Towards the plasma edge, the heat flux decreases steadily, with a notable

Table 3: Summary of cavity calorimeter results for CO₂ at varying specific energy input.

Condition	Q_{tube} [kW]	Q_{nozzle} [kW]	P_{cal} [kW]	\bar{h}_{tot} [MJ/kg]	η_{tot} [-]
CO2#01a	11.31	4.17	30.98 ± 1.52	14.08 ± 0.70	0.193
CO2#01b	11.43	4.17	32.48 ± 1.59	14.76 ± 0.74	0.202
CO2#02	10.14	2.18	35.57 ± 1.72	11.86 ± 0.58	0.222
CO2#03	9.46	1.86	34.49 ± 1.66	9.85 ± 0.48	0.231
CO2#04	8.88	1.38	31.56 ± 1.51	7.89 ± 0.38	0.234

plateau between $r = 40$ mm and $r = 60$ mm. The Pitot measurement shows a prominent off-centered global peak of 466 Pa at 60 mm and a smaller local peak on the plasma jet centerline. It is believed that the off-centered global peak originates from the tangential gas injection in IPG4, which stabilizes the plasma, leading to an increased static pressure at the discharge chamber wall [15]. The radial position of the peak is strongly influenced by the jet expansion and depends on the axial measurement position and the ambient pressure in the tank. The Pitot profile can be described by a double Gaussian distribution, which is drawn as a green line and follows the equation:

$$f(r) = a_1 \exp\left(-\frac{(r-b_1)^2}{2c_1^2}\right) + a_2 \exp\left(-\frac{(r-b_2)^2}{2c_2^2}\right) + d \quad (18)$$

with $a_1 = 2.72 \cdot 10^2$ Pa, $b_1 = 7.9 \cdot 10^{-4}$ m, $c_1 = 4.06 \cdot 10^{-2}$ m, $a_2 = 2.79 \cdot 10^2$ Pa, $b_2 = 6.17 \cdot 10^{-2}$ m, $c_2 = 1.2 \cdot 10^{-2}$ m and $d = 100$ Pa. This characteristic shape will be used in Section 3.2 for the determination of the local mass flux profile.

Based on the measurements of heat flux and Pitot pressure at condition CO2#01b, the radial distribution of the mass-specific enthalpy can be calculated, using Eq. 5. Figure 9 presents the locally measured values. Here, the uncertainty region is indicated by a gray shadow.

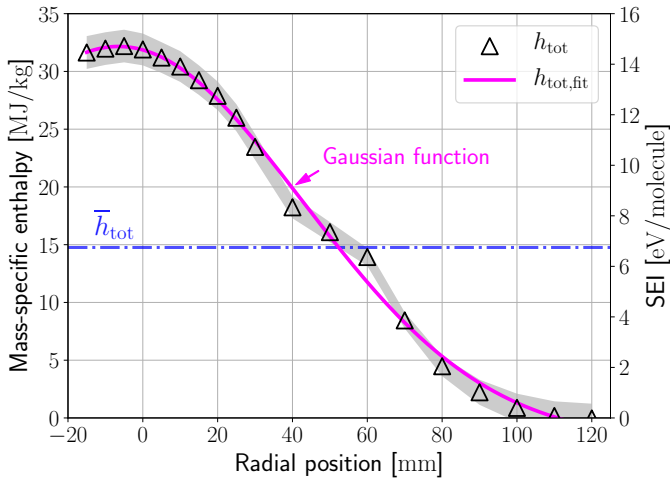


Figure 9: Radial distribution of the mass-specific enthalpy (black triangles) for the condition CO2#01b at $x = 156$ mm, with uncertainty region in gray. The mean enthalpy is indicated as a horizontal blue line. A Gaussian function (magenta) is fitted to the enthalpy data.

The mass-specific enthalpy shows a bell-shaped distribution with a maximum value of 32.2 MJ/kg near the centerline and

negligible enthalpies at the plasma edge. Based on the simulation of thermal splitting (Fig. 5) full dissociation of CO₂ is expected for the inner plasma jet region, i.e., radial positions of $r < 60$ mm. The highest energy efficiencies of approx. 50 % are estimated to be around $r = 70$ mm. The mean mass-specific enthalpy of $\bar{h}_{\text{tot}} = 14.76$ MJ/kg, measured with the cavity calorimeter for CO2#01b, is depicted as a horizontal blue line. Moreover, a Gaussian function, drawn in magenta, is fitted to the enthalpy data. The fit function is in good agreement with the measurements and lies within the uncertainty region for nearly all points. The fit function follows the equation:

$$f(r) = a \exp\left(-\frac{(r-b)^2}{2c^2}\right) + d \quad (19)$$

with $a = 3.42 \cdot 10^7$ J/kg, $b = -6.53 \cdot 10^{-3}$ m, $c = 4.93 \cdot 10^{-2}$ m and $d = -2.01 \cdot 10^6$ J/kg.

The probe measurements show a strong spatial inhomogeneity in specific enthalpy at the test position. On the plasma jet centerline, as well as in the outer parts of the plume, the enthalpy deviates significantly from the mean value. In the following, the influence of this spatial inhomogeneity in specific energy input on the total CO₂ splitting performance will be investigated.

3.2. The influence of inhomogeneity on CO₂ splitting performance

In this section, the influence of spatial enthalpy inhomogeneity on the carbon dioxide conversion and, thus, the energy efficiency of CO₂ splitting is examined by the example of the test condition CO2#01b. To do so, two cases are constructed: First, a theoretical scenario where the mass-specific enthalpy is constant over radius, i.e., at all positions in the plasma jet the enthalpy equals the mean value of $\bar{h}_{\text{tot}} = 14.76$ MJ/kg. Second, the real scenario, where mass flux and enthalpy are inhomogeneously distributed over the plasma jet radius, leading to the mass-specific enthalpy profile in Fig. 9. Although the probe measurements are conducted in the vacuum tank after plasma expansion through the convergent nozzle, it is assumed that the measured specific energy distribution is representative of the inhomogeneities during plasma generation, and thus CO₂ conversion, in the discharge region of the plasma source. This is supported by numerical simulations by Vasil'evskii et al. of an air flow in an inductively coupled plasma (ICP) source similar to the one used in the course of this work [31]. The simulations show that the inhomogeneities in mass-specific enthalpy are introduced during plasma generation in the discharge region

already, before being expanded in the vacuum tank. Thus, the measurements with the double probe in PWK3 are a measure of the inhomogeneous plasma generation process in the generator itself.

The CO₂ conversion is in both cases, homogeneous and inhomogeneous, calculated using Cantera under the assumption of thermodynamic equilibrium (cp. Section 2.3). For IPG4, this is a good approximation, at least for the plasma generation phase inside the generator, as shown in recent work [14]. In the homogeneous case, the carbon dioxide splitting performance can be directly read from Fig. 5. In the case of inhomogeneous enthalpy distribution, the mass distribution in the plasma jet must be known in order to calculate the integral splitting performance. Hence, the mass flux distribution at the test position in the CO₂ plasma jet is determined in the following.

3.2.1. Mass flux determination

To calculate the integral splitting performance in the inhomogeneous case, the mass flux (mass flow rate density) is required, since the measured enthalpy is mass-specific and does not reveal the enthalpy distribution per mass. The mass flux, in cylindrical coordinates (r, φ) , is defined as

$$j_m(r, \varphi) = \frac{d\dot{m}}{dA} \quad (20)$$

with the mass flow rate \dot{m} and the plasma jet cross-sectional area A . Unfortunately, there is no way to directly measure the local mass flux, but the distribution can be reconstructed using the plasma probe measurements presented earlier. In particular, three primary criteria must be met by a suitable mass flux profile:

1. At the plasma edge (R_{\max}) the mass flux is zero:

$$j_m(R_{\max}, \varphi) = 0 \quad (21)$$

2. The mass flux integrated over the plasma jet cross section equals the total mass flow rate:

$$\dot{m} = \int_0^{2\pi} \int_0^{R_{\max}} j_m(r, \varphi) r \, dr \, d\varphi \quad (22)$$

3. The product of mass flux and specific enthalpy integrated over the plasma jet cross-sectional area is equal to the total calorimetric plasma power:

$$P_{\text{cal}} = \int_0^{2\pi} \int_0^{R_{\max}} h_{\text{tot}}(r, \varphi) j_m(r, \varphi) r \, dr \, d\varphi \quad (23)$$

For CO2#01b, the total mass flow rate is known to be $\dot{m} = 2.2 \text{ g/s}$. Moreover, the calorimetric plasma power $P_{\text{cal}} = 32.48 \text{ kW}$ was measured with the cavity calorimeter (Tab. 3). In addition, the radial distribution of the mass specific enthalpy $h_{\text{tot}}(r, \varphi)$ was determined with the double probe (Fig. 9). In the course of this analysis, the Gaussian fit function of the measured enthalpies $h_{\text{tot,fit}}$ is used instead of the single data points, serving as a continuous function in the calculations. Moreover, rotational symmetry is assumed inside the IPG4 plasma jet:

$$h_{\text{tot}} \neq f(\varphi), \quad j_m \neq f(\varphi) \quad (24)$$

With the assumption of rotational symmetry, the Eqs. 21-23 and the probe measurement data, a mass flux profile with three degrees of freedom (DOF), such as simplified Gaussian profiles, can be clearly identified. However, for centered and off-centered Gauss profiles no solution of the mass flux can be found. Thus, it is further assumed that the shape of the radial mass flux distribution is similar to the Pitot pressure profile (Fig. 8), since stagnation pressure and mass flux are closely related to one another. Consequently, the mass flux profile is believed to follow a double Gaussian distribution (Eq. 18). The ratio of the profile widths c_2/c_1 , as well as the height ratio of the two peaks (value of central peak divided by value of off-centered peak) are adopted from the Pitot profile to be 0.3 and 0.735, respectively. Under these conditions, a mass flux distribution can be clearly identified. For CO2#01b the resulting profile is plotted in Fig. 10.

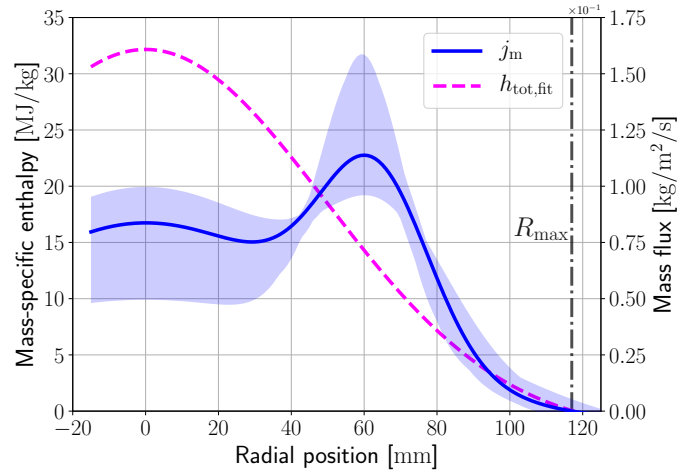


Figure 10: Reconstructed mass flux profile (blue line) for the condition CO2#01b at $x = 156 \text{ mm}$ under the assumption of similarity to the Pitot profile. The Gaussian fit to the enthalpy data is plotted in magenta and the identified plasma edge is printed as a gray vertical line.

At $x = 156 \text{ mm}$ a plasma edge position of $R_{\max} = 117 \text{ mm}$ was determined by examining the double probe results. This value is indicated in the figure. The calculated mass flux profile is plotted as a blue line. The profile follows a double Gaussian distribution with $a_1 = 8.92 \cdot 10^{-2} \text{ kg/m}^2/\text{s}$, $b_1 = 0 \text{ m}$, $c_1 = 4.94 \cdot 10^{-2} \text{ m}$, $a_2 = 7.82 \cdot 10^{-2} \text{ kg/m}^2/\text{s}$, $b_2 = 6.30 \cdot 10^{-2} \text{ m}$, $c_2 = 1.48 \cdot 10^{-2} \text{ m}$ and $d = -5.50 \text{ kg/m}^2/\text{s}$ (cp. Eq. 18). The Gaussian fit of the enthalpy measurement is added in magenta, shifted horizontally to be axially symmetric. The light blue shadow serves as a sensitivity analysis towards the assumed values of c_2/c_1 , the peak ratio and the plasma radius R_{\max} . The colored region includes all solutions of the mass flux profile for $0.15 \leq c_2/c_1 \leq 0.45$, $0.32 \leq \text{peak ratio} \leq 1.0$ and $107 \text{ mm} \leq R_{\max} \leq 127 \text{ mm}$. While in theory an infinite number of double Gaussian mass flux profiles can be found, most of them represent non-physical or unrealistic solutions, like a singularity at the position of mean enthalpy or a significantly higher mass flux on the centerline than at the off-centered peak position. Thus, it is probable that the sensitivity analysis covers a wide range of possible mass flux profiles. Nevertheless, other

shapes than double Gaussian functions, e.g., with more degrees of freedom, could lead to valid solutions, but are not included in this analysis. It has to be noted that the global mass flux peak is close to the position of the mean value of the mass-specific enthalpy for CO2#01b, which supports the choice of the profile shape. This might be due to a superposition of the tangential gas injection in IPG4 and the power coupling close the quartz tube wall due to the skin effect [10].

3.2.2. CO₂ splitting under inhomogeneity

In a last step, the mass flux distribution profile and the measured local mass-specific enthalpy values can be combined to calculate the integral CO₂ conversion and energy efficiency. A comparison to the splitting performance in the case of a homogeneous distribution of enthalpy over plasma radius quantifies the influence of the inhomogeneity. To determine the inhomogeneous splitting performance, the converted mass in the inhomogeneous case, assuming rotational symmetry, is calculated:

$$\chi_{\text{inhom}} = \frac{2\pi}{\dot{m}} \int_0^{R_{\text{max}}} \chi(r) j_m(r) r dr \quad (25)$$

which leads to the energy efficiency in the inhomogeneous case:

$$\eta_{\text{inhom}} = \chi_{\text{inhom}} \cdot \frac{\Delta H_{298}^0 e \cdot N_A}{\bar{h}_{\text{tot}} M_{\text{CO}_2}} \quad (26)$$

The local CO₂ conversion values $\chi(r)$ are determined by feeding the local mass-specific enthalpy $h_{\text{tot,fit}}(r)$ into the thermodynamic equilibrium simulation tool based on Cantera (cp. Section 2.3). This methodology is used in a parameter study, where not only the measured enthalpy profile of CO2#01b $h_{\text{tot,fit}}$, but additional artificial Gaussian enthalpy distributions, varying in their Full Width at Half Maximum (*FWHM*), i.e., their spatial inhomogeneity, are investigated. The smaller the *FWHM* of the enthalpy distribution, the higher is the inhomogeneity. The normalized enthalpy profiles used in the parameter study are plotted in Fig. 11.

For each profile, the peak height and the *FWHM* are chosen so that the bulk enthalpy equals $\bar{h}_{\text{tot}} = 14.76 \text{ MJ/kg}$, which is the calorimetrically measured value for CO2#01b. Moreover, the mass flux distribution is kept constant and equals the earlier determined profile (Fig. 10) for the study. This theoretical parameter study would in reality resemble an experiment, where the mass injection into the generator remains unchanged, while the radial distribution (not the total value) of the applied power is altered. Consequently, the homogeneous comparison case for CO₂ splitting is the same for each distribution. The conversion and energy efficiency in the homogeneous case can be directly extracted from Fig. 5 to be $\chi_{\text{hom}} = 97.1 \%$ and $\eta_{\text{hom}} = 42.2 \%$, respectively. For the inhomogeneous enthalpy distributions, Eqs. 25 and 26 are applied to calculate the CO₂ splitting performance in the case of spatial inhomogeneity. The results of the parameter study are plotted in Fig. 12.

In the figure, the ratio of energy efficiency in the case of inhomogeneous specific energy distribution versus the homogeneous case is plotted as a function of the *FWHM* of the enthalpy distribution, normalized with R_{max} , which is a direct measure

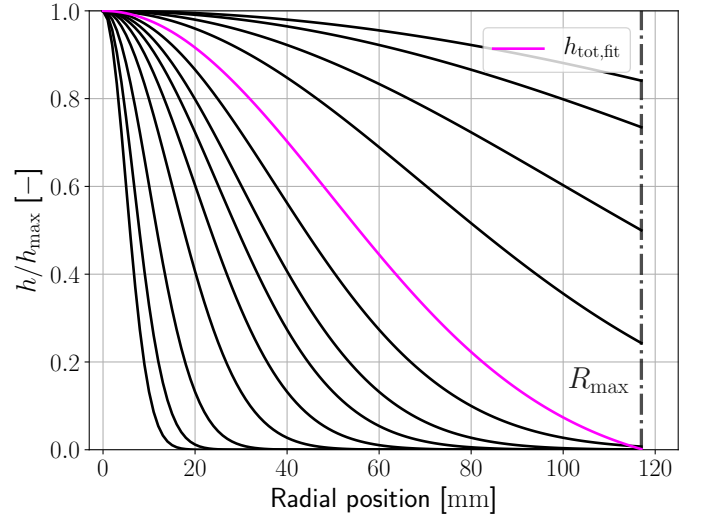


Figure 11: Normalized Gaussian radial enthalpy profiles with varying *FWHM* used in the parameter study. The measured specific enthalpy distribution for CO2#01b is colored in magenta.

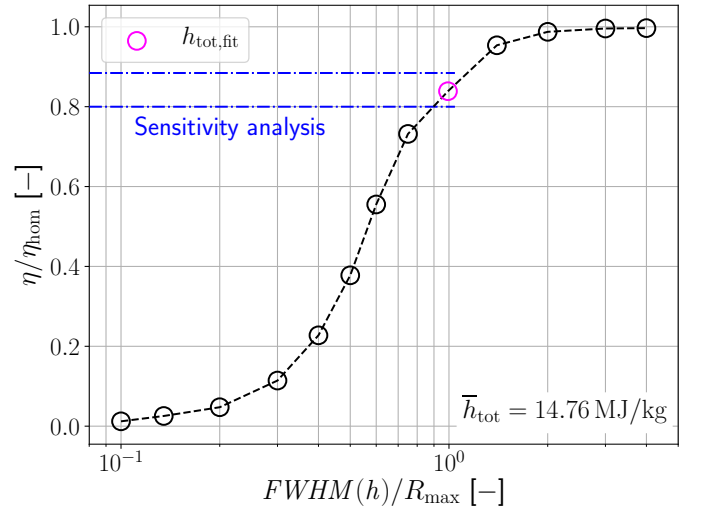


Figure 12: Ratio of inhomogeneous energy efficiency to the homogeneous comparison case as a function of the *FWHM* of the mass-specific enthalpy profile, normalized with R_{max} . Towards the left, the inhomogeneity increases. The ratio of the measured enthalpy distribution (CO2#01b) is colored in magenta. Two horizontal blue lines represent the parameter range of the sensitivity analysis.

of inhomogeneity. It has to be emphasized again that all investigated profiles, in combination with the mass flux distribution, have the same mean enthalpy. Above all, the analysis shows that spatial inhomogeneity in specific enthalpy significantly lowers the CO₂ splitting performance in a plasma jet. This is due to the nonlinear correlation of SEI and the carbon dioxide conversion (cp. Fig. 5). Moreover, it can be seen that the higher the inhomogeneity, the lower the splitting performance for the same mean mass-specific enthalpy, i.e., the same SEI. At large *FWHM*, the Gaussian specific enthalpy profile approaches a constant radial distribution, which results in an asymptotic behavior towards the homogeneous case. For CO2#01b, the *FWHM* is in the order of the plasma jet ra-

dius. The corresponding conversion and energy efficiency are $\chi_{01b} = 81.5\%$ and $\eta_{01b} = 35.4\%$, respectively. As a result, the inhomogeneous distribution of mass-specific enthalpy in IPG4 lowers the carbon dioxide splitting performance by 16%.

The blue horizontal lines in Fig. 12 indicate the sensitivity of the CO₂#01b splitting performance to changes in the mass flux profile. The plotted result space corresponds to the blue-shaded region in Fig. 10. Although the mass flux profile is altered strongly in the sensitivity analysis, the influence on the splitting performance is quite limited (approx. 10%). The reason for this is that a large fraction of the mass flux is situated in outer regions of the plasma jet, where the mass flux variation is comparably small (cp. Fig. 10). Moreover, the mean enthalpy in the study of $\bar{h}_{tot} = 14.76$ MJ/kg is in a near linear region regarding the energy efficiency (cp. Fig. 5). This region is characterized by robustness to inhomogeneities in the mass-specific enthalpy.

The inhomogeneities encountered in IPG4 are caused by the superposition of gas injection near the quartz tube edge and the radially inhomogeneous power distribution due to the skin effect [15]. Therefore, the decrease in splitting performance is mostly defined by geometric parameters, like the injector placement, and the operational frequency. Since all conditions introduced in this paper (CO₂#01-CO₂#04) use the same plasma generator, operated at the same frequency, it is expected that the inhomogeneities are similar. Consequently, by changing the operating parameters the overall CO₂ splitting performance can be optimized, i.e., by adjusting the mean mass-specific enthalpy, but the inhomogeneity, leading to lower efficiencies, is not believed to be affected strongly. It has to be stated that this is only true as long as the discharge mode (inductive 'mode 3', cp. [32]) remains unchanged.

4. Conclusion and outlook

In this work, the specific energy inhomogeneity in the high-power carbon dioxide plasma jet of the inductive plasma generator IPG4 was determined experimentally. Its influence on the CO₂ splitting performance was quantified, showing a negative correlation between specific enthalpy inhomogeneity and CO₂ conversion, and thus energy efficiency.

Using a cavity calorimeter, calorimetric CO₂ plasma powers were measured for five different operating conditions in plasma wind tunnel PWK3. Moreover, total generator efficiencies of IPG4 in the range of 19.3 – 23.4% were determined. A heat flux-Pitot double probe was applied to resolve the radial distribution of the mass-specific enthalpy for the condition CO₂#01b ($P_A = 160$ kW, $\dot{m}_{CO_2} = 2.2$ g/s). The measurements showed a strong inhomogeneity in specific energy at the test position of $x = 156$ mm.

Based on the probe measurements, a radial mass flux profile was calculated. Here, a double Gaussian distribution, similar to the Pitot pressure, was assumed. In a parameter study, the influence of inhomogeneity in the mass-specific enthalpy distribution on the carbon dioxide splitting performance in thermodynamic equilibrium was quantified. The analysis revealed that specific energy inhomogeneities lower the CO₂ conversion, and

consequently the energy efficiency, significantly, compared to a fully homogeneous distribution over plasma radius. Although this work only considers thermal CO₂ splitting, it is expected that the presented results qualitatively apply for non-thermal carbon dioxide dissociation as well, as long as some form of nonlinearity between SEI and the CO₂ conversion occurs.

The shown influence of inhomogeneity on plasma-based CO₂ splitting should be considered in future designs of plasma sources, but also for the application of diagnostics and in plasma modeling, because splitting performance can be, and is, lost due to inhomogeneities. As a consequence, only local measurements are able to reveal the true potential of a plasma source with regards to plasma-based CO₂ conversion.

In future work, the determination of the local species composition in the plasma jet in PWK3 by optical emission spectroscopy (OES) is planned. This is to support or disprove the assumption of thermal CO₂ conversion in the plasma generator IPG4.

Funding

This work was supported by the German Academic Scholarship Foundation (Studienstiftung des Deutschen Volkes); and the Friedrich und Elisabeth Boysen-Stiftung.

References

- [1] IPCC, 2022, Summary for policymakers [H.-O. Pörtner, D.C. Roberts, E.S. Poloczanska, K. Mintenbeck, M. Tignor, A. Alegría, M. Craig, S. Langsdorf, S. Löschke, V. Möller, A. Okem (eds.)], in: *Climate Change 2022: Impacts, Adaptation, and Vulnerability. Contribution of Working Group II to the Sixth Assessment Report of the Intergovernmental Panel on Climate Change* [H.-O. Pörtner, D.C. Roberts, M. Tignor, E.S. Poloczanska, K. Mintenbeck, A. Alegría, M. Craig, S. Langsdorf, S. Löschke, V. Möller, A. Okem, B. Rama (eds.)], Cambridge University Press, Cambridge, UK and New York, NY, USA, 2022, pp. 3–33. doi:10.1017/9781009325844.001.
- [2] A. Bogaerts, G. Centi, Plasma technology for CO₂ conversion: a personal perspective on prospects and gaps, *Front Energy Res* 8 (2020) 111. doi:10.3389/fenrg.2020.00111.
- [3] R. Snoeckx, A. Bogaerts, Plasma technology – a novel solution for CO₂ conversion?, *Chem Soc Rev* 46 (19) (2017) 5805–5863. doi:10.1039/C6CS00066E.
- [4] A. George, B. Shen, M. Craven, Y. Wang, D. Kang, C. Wu, X. Tu, A review of non-thermal plasma technology: A novel solution for CO₂ conversion and utilization, *Renew Sust Energy Rev* 135 (2021) 109702. doi:10.1016/j.rser.2020.109702.
- [5] A. van de Steeg, P. Viegas, A. Silva, T. Butterworth, A. van Bavel, J. Smits, P. Diomede, M. van de Sanden, G. van Rooij, Redefining the microwave plasma-mediated CO₂ reduction efficiency limit: the role of O–CO₂ association, *ACS Energy Lett* 6 (8) (2021) 2876–2881. doi:10.1021/acsenerylett.1c01206.
- [6] V. Vermeiren, A. Bogaerts, Supersonic microwave plasma: potential and limitations for energy-efficient CO₂ conversion, *J Phys Chem C* 122 (45) (2018) 25869–25881. doi:10.1021/acs.jpcc.8b08498.
- [7] A. Hecimovic, A. Federico, E. Carbone, U. Fantz, Enhancement of CO₂ conversion in microwave plasmas using a nozzle in the effluent, *J CO₂ Util* 57 (2022) 101870. doi:10.1016/j.jcou.2021.101870.
- [8] A. J. Wolf, F. Peeters, P. Groen, W. Bongers, M. Van De Sanden, CO₂ conversion in nonuniform discharges: disentangling dissociation and recombination mechanisms, *J Phys Chem C* 124 (31) (2020) 16806–16819. doi:10.1021/acs.jpcc.0c03637.

- [9] P. Viegas, L. Vialetto, A. Wolf, F. Peeters, P. Groen, T. Righart, W. Bongers, M. Van de Sanden, P. Diomede, Insight into contraction dynamics of microwave plasmas for CO₂ conversion from plasma chemistry modelling, *Plasma Sources Sci Technol* 29 (10) (2020) 105014. doi:10.1088/1361-6595/abb41c.
- [10] G. Herdrich, Aufbau, qualifikation und charakterisierung einer induktiv beheizten plasmawindkanalanlage zur simulation atmosphärischer eintrittsmänöver, Ph.D. thesis, University of Stuttgart (2004). doi:10.18419/opus-3690.
- [11] S. Loehle, S. Lein, C. Eichhorn, G. Herdrich, M. Winter, Spectroscopic investigation of an inductively heated CO₂ plasma for Mars entry simulation, *J Tech Phys* 50 (3) (2009) 233–246.
- [12] T. Marynowski, S. Loehle, S. Fasoulas, A. Meindl, F. Zander, Aerothermodynamic investigation of inductively heated CO₂ plasma flows for Mars entry testing, in: 45th AIAA Plasmadynamics and Lasers Conference, American Institute of Aeronautics and Astronautics, Atlanta, GA, USA, 2014, pp. 1–19. doi:10.2514/6.2014-2537.
- [13] B. Massuti-Ballester, G. Herdrich, Experimental methodology to assess atomic recombination on high-temperature materials, *J Thermophys Heat Trans* 32 (2) (2018) 353–368. doi:10.2514/1.T5132.
- [14] H. Burghaus, C. F. Kaiser, A. S. Pagan, S. Fasoulas, G. Herdrich, Aerothermodynamic characterization of an inductively generated CO₂ plasma by laser absorption spectroscopy, Manuscript submitted for publication (2023).
- [15] G. Herdrich, M. Auweter-Kurtz, H. Kurtz, T. Laux, M. Winter, Operational behavior of inductively heated plasma source IPG3 for entry simulations, *J Thermophys Heat Trans* 16 (3) (2002) 440–449. doi:10.2514/2.6698.
- [16] H. Burghaus, G. Herdrich, S. Fasoulas, Derivation of species distribution in inductively heated CO₂ plasma via automated spectral fitting, *Vacuum* 184 (2021) 109901. doi:https://doi.org/10.1016/j.vacuum.2020.109901.
- [17] S. Loehle, F. Zander, M. Eberhart, T. Hermann, A. Meindl, B. Massuti-Ballester, D. Leiser, F. Hufgard, A. S. Pagan, G. Herdrich, et al., Assessment of high enthalpy flow conditions for re-entry aerothermodynamics in the plasma wind tunnel facilities at IRS, CEAS Space J (2021) 1–12doi:10.1007/s12567-021-00396-y.
- [18] S. Pidan, M. Auweter-Kurtz, G. Herdrich, M. Fertig, Recombination coefficients and spectral emissivity of silicon carbide-based thermal protection materials, *J Thermophys Heat Trans* 19 (4) (2005) 566–571. doi:10.2514/1.12814.
- [19] C. F. Kaiser, H. Burghaus, G. Herdrich, In-situ emissivity assessment of grade 5 titanium in high-enthalpy flows for catalysis investigations, in: 73rd International Astronautical Congress (IAC), International Astronautical Federations, Paris, France, 2022.
- [20] J. G. Marvin, R. B. Pope, Laminar convective heating and ablation in the Mars atmosphere., *AIAA J* 5 (2) (1967) 240–248. doi:10.2514/3.3948.
- [21] E. V. Zoby, Empirical stagnation-point heat-transfer relation in several gas mixtures at high enthalpy levels, Technical Note 4799, National Aeronautics and Space Administration (1968).
- [22] ASTM International, Standard test method for calculation of stagnation enthalpy from heat transfer theory and experimental measurements of stagnation-point heat transfer and pressure, Tech. Rep. E 637–05 (2005).
- [23] G. Herdrich, T. Marynowski, M. Dropmann, S. Fasoulas, Mars and Venus entry simulation capabilities of IRS plasma wind tunnel PWK3, *Appl Phys Res* 4 (1) (2012). doi:10.18419/opus-3871.
- [24] D. G. Goodwin, R. L. Speth, H. K. Moffat, B. W. Weber, Cantera: An object-oriented software toolkit for chemical kinetics, thermodynamics, and transport processes, <https://www.cantera.org>, version 2.4.0 (2018). doi:10.5281/zenodo.4527812.
- [25] J. D. Anderson Jr, Fundamentals of Aerodynamics, 3rd Edition, McGraw-Hill, New York, 2001.
- [26] M. Dropmann, G. Herdrich, R. Laufer, D. Puckert, H. Fulge, S. Fasoulas, J. Schmoke, M. Cook, T. W. Hyde, A new inductively driven plasma generator (IPG6)—setup and initial experiments, *IEEE Trans Plasma Sci* 41 (4) (2013) 804–810. doi:10.1109/TPS.2012.2237524.
- [27] C. R. Harris, K. J. Millman, S. J. van der Walt, R. Gommers, P. Virtanen, D. Cournapeau, E. Wieser, J. Taylor, S. Berg, N. J. Smith, R. Kern, M. Picus, S. Hoyer, M. H. van Kerkwijk, M. Brett, A. Hal-dane, J. Fernández del Río, M. Wiebe, P. Peterson, P. Gérard-Marchant, K. Sheppard, T. Reddy, W. Weckesser, H. Abbasi, C. Gohlke, T. E. Oliphant, Array programming with NumPy, *Nature* 585 (2020) 357–362. doi:10.1038/s41586-020-2649-2.
- [28] J. D. Hunter, Matplotlib: A 2d graphics environment, *Comput Sci Eng* 9 (3) (2007) 90–95. doi:10.1109/MCSE.2007.55.
- [29] P. Virtanen, R. Gommers, T. E. Oliphant, M. Haberland, T. Reddy, D. Cournapeau, E. Burovski, P. Peterson, W. Weckesser, J. Bright, S. J. van der Walt, M. Brett, J. Wilson, K. J. Millman, N. Mayorov, A. R. J. Nelson, E. Jones, R. Kern, E. Larson, C. J. Carey, Í. Polat, Y. Feng, E. W. Moore, J. VanderPlas, D. Laxalde, J. Perktold, R. Cimrman, I. Henriksen, E. A. Quintero, C. R. Harris, A. M. Archibald, A. H. Ribeiro, F. Pedregosa, P. van Mulbregt, SciPy 1.0 Contributors, SciPy 1.0: Fundamental Algorithms for Scientific Computing in Python, *Nat Methods* 17 (2020) 261–272. doi:10.1038/s41592-019-0686-2.
- [30] W. McKinney, et al., Data structures for statistical computing in python, in: Proceedings of the 9th Python in Science Conference, Vol. 445, Austin, TX, 2010, pp. 51–56.
- [31] S. Vasil’evskii, A. Kolesnikov, A. Bryzgalov, S. Yakush, Numerical simulation of equilibrium air plasma flow in the induction chamber of a high-power plasmatron, *Contin Mech Thermodyn* (2023) 1–13doi:10.1007/s00161-023-01192-1.
- [32] R. Georg, A. Chadwick, B. Dally, G. Herdrich, Power efficiency estimation of an inductive plasma generator using propellant mixtures of oxygen, carbon-dioxide and argon, *Acta Astronaut* 179 (2021) 536–545. doi:10.1016/j.actaastro.2020.11.020.